

A Retrieval of Tropical Latent Heating Using the 3D Structure of Precipitation Features

FIAZ AHMED AND COURTNEY SCHUMACHER

Department of Atmospheric Sciences, Texas A&M University, College Station, Texas

ZHE FENG AND SAMSON HAGOS

Pacific Northwest National Laboratory, Richland, Washington

(Manuscript received 21 January 2015, in final form 1 October 2015)

ABSTRACT

Radar-based latent heating retrievals typically apply a lookup table (LUT) derived from model output to surface rain amounts and rain type to determine the vertical structure of heating. In this study, a method has been developed that uses the size characteristics of precipitating systems (i.e., area and mean echo-top height) instead of rain amount to estimate latent heating profiles from radar observations. This technique [named the convective–stratiform area (CSA) algorithm] leverages the relationship between the organization of convective systems and the structure of latent heating profiles and avoids pitfalls associated with retrieving accurate rainfall information from radars and models. The CSA LUTs are based on a high-resolution regional model simulation over the equatorial Indian Ocean. The CSA LUTs show that convective latent heating increases in magnitude and height as area and echo-top heights grow, with a congestus signature of midlevel cooling for less vertically extensive convective systems. Stratiform latent heating varies weakly in vertical structure, but its magnitude is strongly linked to area and mean echo-top heights. The CSA LUT was applied to radar observations collected during the DYNAMO/Cooperative Indian Ocean Experiment on Intraseasonal Variability in the Year 2011 (CINDY2011)/ARM MJO Investigation Experiment (AMIE) field campaign, and the CSA heating retrieval was generally consistent with other measures of heating profiles. The impact of resolution and spatial mismatch between the model and radar grids is addressed, and unrealistic latent heating profiles in the stratiform LUT, namely, a low-level heating peak, an elevated melting layer, and net column cooling, were identified. These issues highlight the need for accurate convective–stratiform separations and improvement in PBL and microphysical parameterizations.

1. Introduction

Latent heat released during moist convective processes can trigger a slew of local and large-scale phenomena. Local changes such as buoyancy perturbations manifest themselves as gravity waves that can engender further convection leading to mesoscale organization (Mapes 1993; Lac and Lafore 2002). The condensational heating from organized convective systems can determine the seasonal and intraseasonal sources of tropical variability, as demonstrated by idealized modeling studies (e.g., Gill

1980; Hartmann et al. 1984). Major weather systems across the tropics and the extratropics are fueled by latent heat: the East Asian summer monsoon (Jin et al. 2013), the African monsoon (Hagos and Zhang 2010), mid-latitude cyclones (Stoelinga 1996; Willison et al. 2013), and tropical waves and the Madden–Julian oscillation (Chen and Yen 1991; Li et al. 2009; Lappen and Schumacher 2012).

The vertical profile of latent heating is a representation of the convecting atmosphere and a useful proxy for large-scale vertical velocities in the tropics, with the magnitude of heating being dominated by condensational processes (Houze 1982, 1989). The influences of large-scale synoptic and planetary wave features and local forcings such as the diurnal cycle can also manifest themselves in the local heating

Corresponding author address: Fiaz Ahmed, Department of Atmospheric Sciences, Texas A&M University, 3150 TAMU, College Station, TX 77843-3150.
E-mail: fiaz.500@tamu.edu

profiles (Schumacher et al. 2007). Accurate retrievals of latent heating are therefore useful to study convection and its associated circulations.

Latent heating associated with convection manifests itself as dynamical perturbations rather than temperature changes (Mapes and Houze 1995), making a direct measurement of latent heating difficult. Reanalysis data, while extensive in coverage, rely heavily on the parent model when observations are scarce and are mainly derived from parameterized cumulus and radiative processes. As a result, the vertical profiles of heating from reanalyses do not always agree with sounding budgets (Hagos et al. 2010; Ling and Zhang 2011) or Tropical Rainfall Measuring Mission (TRMM) satellite retrievals (Chan and Nigam 2009; Jiang et al. 2011). Therefore, reliable estimates of latent heating must be inferred from other measurable quantities like radar reflectivity or rainfall.

Most existing latent heating retrieval methods utilize certain unique properties of tropical convection. Broadly speaking, tropical precipitation can be reduced into two mutually exclusive categories: convective and stratiform, with each category possessing a canonical heating profile (Houze 1997). Stratiform rain processes warm the troposphere at upper levels and cool at lower levels. Deep convective rain processes warm the entire troposphere with a heating peak at midlevels, while shallower convection has a heating peak in the lower troposphere (Schumacher et al. 2004). The bulk of the variance in the vertical structure of tropical latent heating can be explained by a composite of bottom- and middle-heavy convective-like profiles and top-heavy stratiform-like profiles (Zhang and Hagos 2009; Hagos 2010). Thus, several latent heating retrieval algorithms utilize the prior knowledge of convective and stratiform rain separation and the output of heating from cloud models (Tao and Simpson 1989; Tao et al. 1993b).

Multiple latent heating retrieval algorithms exist for products from the TRMM satellite (see review in Tao et al. 2006). For example, Precipitation Radar (PR) observations are used by the convective–stratiform heating (CSH) algorithm (Tao et al. 1993a, 2010), which uses information about surface precipitation rates, the amount of stratiform versus convective rain, and whether the cloud systems are over ocean or land. A lookup table (LUT) generated by a cloud-resolving model (CRM) then provides the convective and stratiform heating profiles. TRMM Microwave Imager (TMI) observations are utilized by the hydrometeor heating (HH; Yang and Smith 1999) and trained radiometer (TRAIN; Olson et al. 1999, 2006; Greco and Olson 2006) algorithms, which also use

CRM-derived LUTs to retrieve vertical heating profiles based on microwave radiative characteristics. The TRMM approach that is most similar to the technique described in this study is the spectral latent heating (SLH) algorithm (Shige et al. 2004), in which information about surface rain, the convective–stratiform separation, the melting layer, and precipitation-top height from a CRM are used to generate a LUT of latent heating profiles and applied to the PR observations.

Schumacher et al. (2004) created a simpler LUT meant to be applied to satellite or ground-based radar. Their method uses convective–stratiform rain information (including from shallow convection) and assumes an idealized heating profile for each rain type. These three idealized profiles were composited from long-term observational studies of vertical motion and diabatic heating in the tropics and are not based on CRM output. Convective and stratiform rain can almost completely determine the large-scale dynamical character of the tropical atmosphere (Mapes and Houze 1995). Therefore, this method works well in estimating the mean latent heating profile averaged over space and time scales representative of mesoscale storm processes (Schumacher et al. 2007).

Because all of the above radar-based latent heating retrievals are dependent on surface rainfall, estimates of which suffer from a number of potential errors (Austin 1987; Houze et al. 2004), and latent heating associated with convective systems is “felt” by the atmosphere much more broadly than in a precipitating column, we introduce a latent heating algorithm that circumvents pixel-based radar rainfall retrievals. Rather, our approach is to estimate latent heating from radar echo area coverage rather than rainfall, where contiguous pixels are grouped into clusters. This procedure increases the representativeness and reduces the error in the sample by reducing the variations in individual pixels. The area paradigm captures the spectrum of convective organization from individual cumulus clouds to mesoscale convective systems and has the potential to be applied across a wide range of regions and platforms.

2. Observations and model configuration

We utilize observations and a 20-day-long regional model simulation from the Dynamics of the Madden–Julian Oscillation (MJO) (DYNAMO), the Cooperative Indian Ocean Experiment on Intraseasonal Variability in the Year 2011 (CINDY2011), and the Atmospheric Radiation Measurement (ARM) MJO Investigation Experiment (AMIE) field campaigns (DYNAMO/CINDY2011/AMIE; hereinafter referred

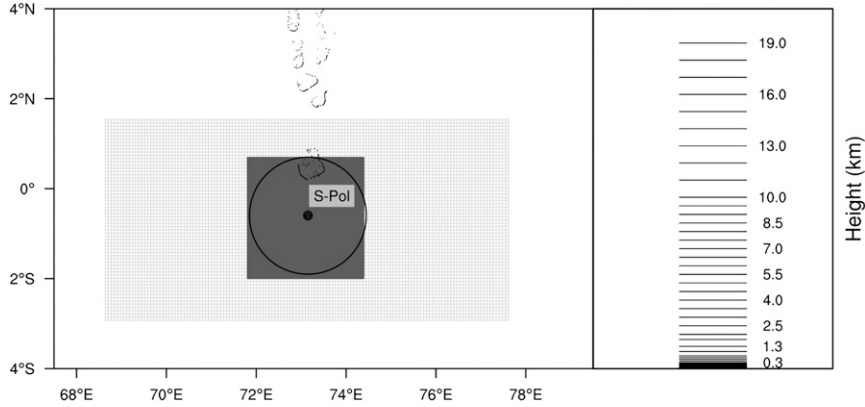


FIG. 1. (left) The Maldives in the Indian Ocean with the WRF domain (outer gray box) and the S-PolKa radar-scale domain (inner gray box), and (right) the WRF vertical resolution. S-PolKa was located on Addu Atoll, the farthest south of the Maldives. The black circle represents the 150-km radius from S-PolKa.

to as DYNAMO), which took place over the equatorial Indian Ocean from October 2011 to March 2012 to better understand and forecast the initiation of the MJO (Yoneyama et al. 2013). The field deployment consisted of numerous observational platforms, although we focus on measurements made with the National Center for Atmospheric Research S-PolKa radar, a dual-frequency (S and Ka band), dual-polarimetric Doppler radar that was located at Addu Atoll, Maldives (Fig. 1).

We also use profiles of the apparent heat source Q_1 retrieved from the DYNAMO sounding and surface rainfall data on Addu Atoll, supplemented by reanalysis information surrounding the atoll. This retrieval is based on the variational analysis approach of Zhang and Lin (1997). Variational analysis minimizes the sampling errors in the sounding data (Mapes et al. 2003) by constraining the sounding observations to conserve column-integrated mass, momentum, energy, and moisture (Zhang et al. 2001). The Q_1 used in this study was calculated as an average over a 300-km domain (see the circle in Fig. 1) centered on the DOE ARM mobile facility on Addu Atoll and was constrained by the S-PolKa near-surface rainfall estimates.

The equation for Q_1 at any vertical level in the troposphere is from Yanai et al. (1973):

$$Q_1 = \frac{\partial \bar{s}}{\partial t} + \overline{\nabla \cdot (s\mathbf{V})} + \frac{\partial(\bar{s}\bar{\omega})}{\partial p} \quad (1)$$

$$= Q_R + L(c - e) - \frac{\partial(\overline{s'\omega'})}{\partial p}, \quad (2)$$

where s is the dry static energy of the atmosphere, \mathbf{V} is the horizontal wind velocity, Q_R is the net column radiative heating of the atmosphere, $L(c - e)$ is the net

column latent heating associated with condensational and evaporative processes, and $s'\omega'$ is the vertical eddy transport of s . The overbar stands for horizontal area averaging, and the primes indicate fluctuations about the mean. Equation (2) can be rearranged as

$$Q_1 - Q_R = L(c - e) - \frac{\partial(\overline{s'\omega'})}{\partial p}, \quad (3)$$

where $Q_1 - Q_R$ equals the sum of the latent heat released and the vertical eddy transport of sensible heat. In the tropics, the net effect of radiation is to cool the troposphere by 1–2 K day⁻¹ (see Fig. 1 in Mapes 2000). The vertical eddy transport of sensible heat is largely positive in mesoscale convective systems (Houze 1982), though it can be negligible in mesoscale convective systems with widespread anvil (Johnson and Young 1983; Yanai and Johnson 1993). The Q_R and $\partial(\overline{s'\omega'})/\partial p$ terms will therefore offset each other and the estimate of

TABLE 1. Model setup.

Simulation period	1–20 Nov 2011
Horizontal resolution	500 m
Microphysics schemes	Modified Thompson (increase raindrop breakup efficiency; Hagos et al. 2014)
Lateral and surface forcing	ERA-Interim 6-hourly analysis
PBL scheme	Mellor–Yamada–Janjić (Janjić 2001)
Surface scheme	Monin–Obukhov–Janjić (Janjić 2001)
Longwave radiation scheme	Rapid Radiative Transfer Model for GCMs (RRTMG; Iacono et al. 2000)
Shortwave radiation scheme	Dudhia (1989)

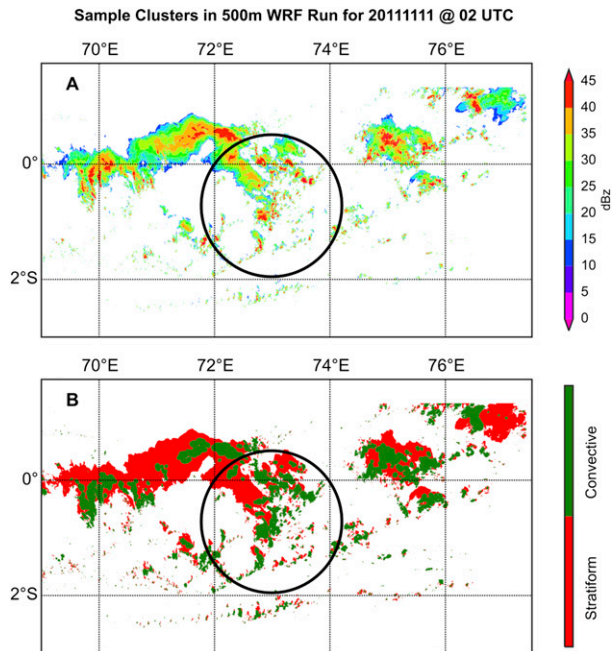


FIG. 2. Example grouping of convective and stratiform reflectivity regions and clusters in the WRF domain for 0200 UTC 11 Nov 2011. The approximate range of the S-Pol surveillance scan is indicated by the circle to show the scale of the clusters.

latent heating using $L(c - e)$ is thus likely to be closer to Q_1 than $Q_1 - Q_R$.

The Advanced Research Weather Research and Forecasting (WRF) Model, version 3.4.1, was used to generate the latent heating LUT. The utility of this

model has been described and demonstrated in Hagos and Leung (2011) for high-resolution regional modeling of the MJO. This version of the model has a forward radar simulator that can simulate S-band (10-cm wavelength) reflectivity based on input hydrometeor size distribution following Smith (1984), which is generated by the model microphysics scheme. The radar simulator used in this model only utilizes precipitating hydrometeors (rain, graupel, and snow) in estimating the reflectivity, thus neglecting the nonprecipitating cloud ice and cloud liquid water (Hagos et al. 2014). The microphysics parameterization is the Thompson scheme (Thompson et al. 2008) but with modified raindrop breakup parameters to improve model-simulated radar reflectivity from precipitating clouds and cold pool statistics. The results pertaining to the use of different microphysics schemes and their effect on the WRF precipitating cloud statistics are detailed in Hagos et al. (2014). Though the model has biases in estimating the rain amount, the biases do not necessarily hinder the construction of the algorithm because we look to exploit the relationship between the model-simulated reflectivity and latent heating profiles.

The model was run with 500-m horizontal resolution and 40 vertical levels over a $4.5^\circ \times 9^\circ$ domain covering a large area of the near-equatorial central Indian Ocean (Fig. 1). Sensitivity tests were also performed with a 2-km horizontal resolution run. The simulation period was from 2 to 20 November 2011, and the model has been shown to adequately capture cloud statistics and cold pools associated with precipitation and to allow comparison with the observations obtained from DYNAMO

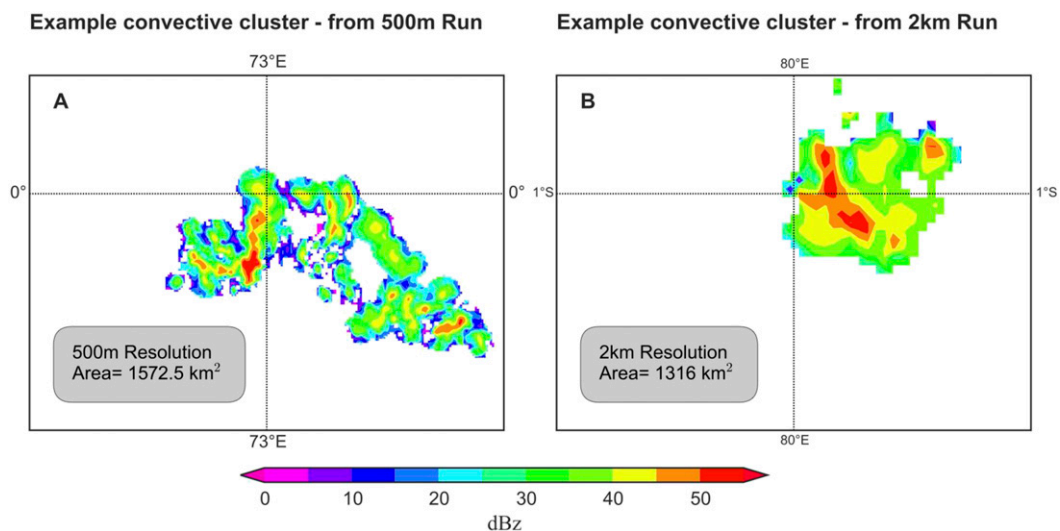


FIG. 3. Reflectivity (dBZ) at 2.5 km for two sample convective clusters of similar size from the (a) 500-m and (b) 2-km runs. Note that the most intense part of the convective cluster is larger in the 2-km run.

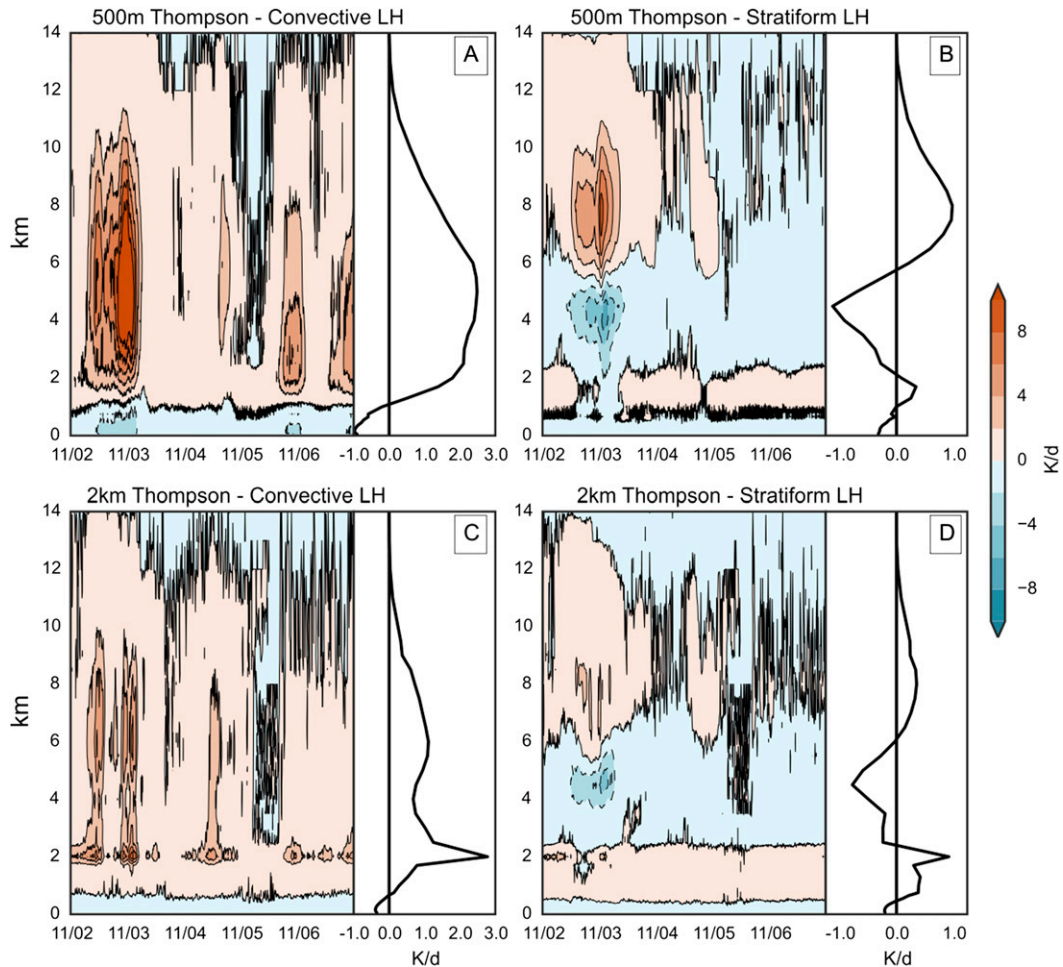


FIG. 4. Example 5-day time series and time-averaged latent heating profiles (K day^{-1}) for the (a) 500-m convective, (b) 500-m stratiform, (c) 2-km convective, and (d) 2-km stratiform clusters. All of the heating profiles are averaged over the same domain, which is indicated by the dark gray shading in Fig. 1.

(Hagos et al. 2014; Feng et al. 2015). The boundaries of the model domain and the sea surface temperature are forced with the ERA-Interim 6-hourly analysis. The other parameterization schemes are listed in Table 1.

3. Algorithm description

Reflectivity data from the WRF radar simulator were used to partition every raining pixel (i.e., reflectivity > 5 dBZ at 2.5 km) in the model into convective and stratiform categories using the method of Steiner et al. (1995). The Steiner et al. algorithm differentiates individual convective and stratiform pixels based on the absolute magnitude and peakedness of the horizontal reflectivity field at a single height (2.5 km in this case). The raining pixels in the model were then grouped into clusters, where a cluster is defined as an area of contiguous reflectivity of the same category (convective or

stratiform; Fig. 2). Before describing the construction of the heating algorithm LUTs, we first explore the sensitivity of the model output to horizontal resolution.

Bryan and Morrison (2012) pointed out the impact of higher resolution on the strength of the convective cells in their WRF squall-line simulation. They showed that for an increase in horizontal resolution, the convective updrafts and cell area decreased in size accompanied by greater occurrence of cloud water evaporation in the downdrafts and cloud edges. We observed the same phenomenon in our model runs, which is illustrated in Fig. 3. The convective cluster in the 500-m run has a greater areal coverage of weak convection than the 2-km convective cluster. This means that 500-m convective cluster possesses weaker area-averaged latent heating than the 2-km cluster. This mismatch influenced our area-based latent heating retrieval when the algorithm was applied to a radar grid that had a 2-km

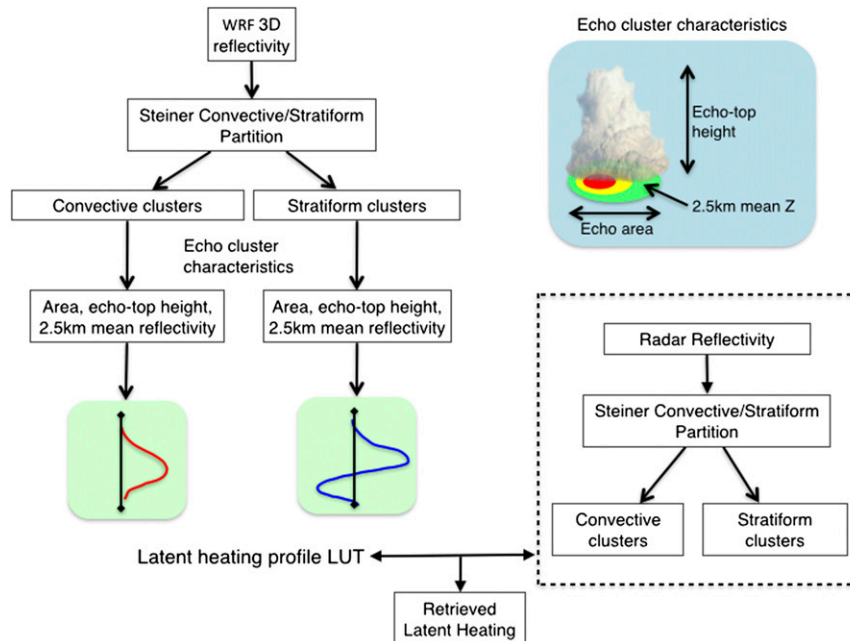


FIG. 5. A schematic describing the flow of the CSA algorithm along with the radar echo cluster characteristics.

horizontal resolution by producing weaker convective heating. To rectify this issue in the 500-m run, we only included convective pixels in the cluster whose 2.5-km reflectivity value was greater than 50% of the maximum reflectivity in the cluster. We note that this modification would depend on the resolution of the radar grid to which the retrieval algorithm is being applied. Since radar data are commonly produced on a 2-km Cartesian grid, this particular version of the algorithm has been tuned for use on a 2-km radar grid.

Figure 4 shows a 5-day time series of the area-averaged heating profile derived directly from the model physics for the convective and stratiform rain clusters in the 500-m and 2-km runs over the dark gray area in Fig. 1. The time-averaged heating profile is attached to each time series. The 5-day period occurred during the suppressed phase of the MJO when large MCSs were largely absent. While the two time series have similar timing in peaks of heating, the vertical structure is quite different. For example, the 500-m convective heating is stronger and more vertically extensive while the 2-km run has a persistent low-level convective heating peak at 2 km that is much less evident in the 500-m run (Figs. 4a,c). The low-level heating is present in both models in weak stratiform clusters, but decreases in the 500-m run relative to the 2-km run (Figs. 4b,d).

About 31% of the model pixels that were classified as stratiform by the Steiner et al. algorithm possessed

heating at low levels. While shallow convection can sometimes be embedded in a stratiform rain region, this is not common in the tropics because of the evaporatively driven mesoscale descent (Brown 1979) below the mid-level cloud base and the depressed mixed layer (e.g., Zipser 1977; Houze and Betts 1981; Johnson and Young 1983). Thus it seems improbable that the subsiding and unsaturated downdrafts of the stratiform cloud cluster could consistently support low-level convection. There are two possibilities to explain the low-level stratiform heating peak. One is that the Steiner et al. algorithm is incorrectly classifying convective pixels as stratiform and we show below that this is likely the case for clusters of small areal extent. However, some clusters with low-level heating remain in the stratiform category after areal extent is considered, which suggests that this heating peak may be an artifact of subgrid processes that are dependent on model processes such as the microphysics or PBL parameterization. The low-level peak was also present when the Morrison microphysics scheme was used for the 2-km run. To further explore the cause of this feature, we performed a heat budget analysis for the boundary layer (not shown) and found that the low-level heating is primarily balanced by the vertical eddy fluxes. This suggests that excessive surface fluxes are found in the model, possibly associated with the PBL and surface schemes. The model SSTs are also fixed and do not respond to changing winds. A combination of all these factors could be the cause of this egregious feature.

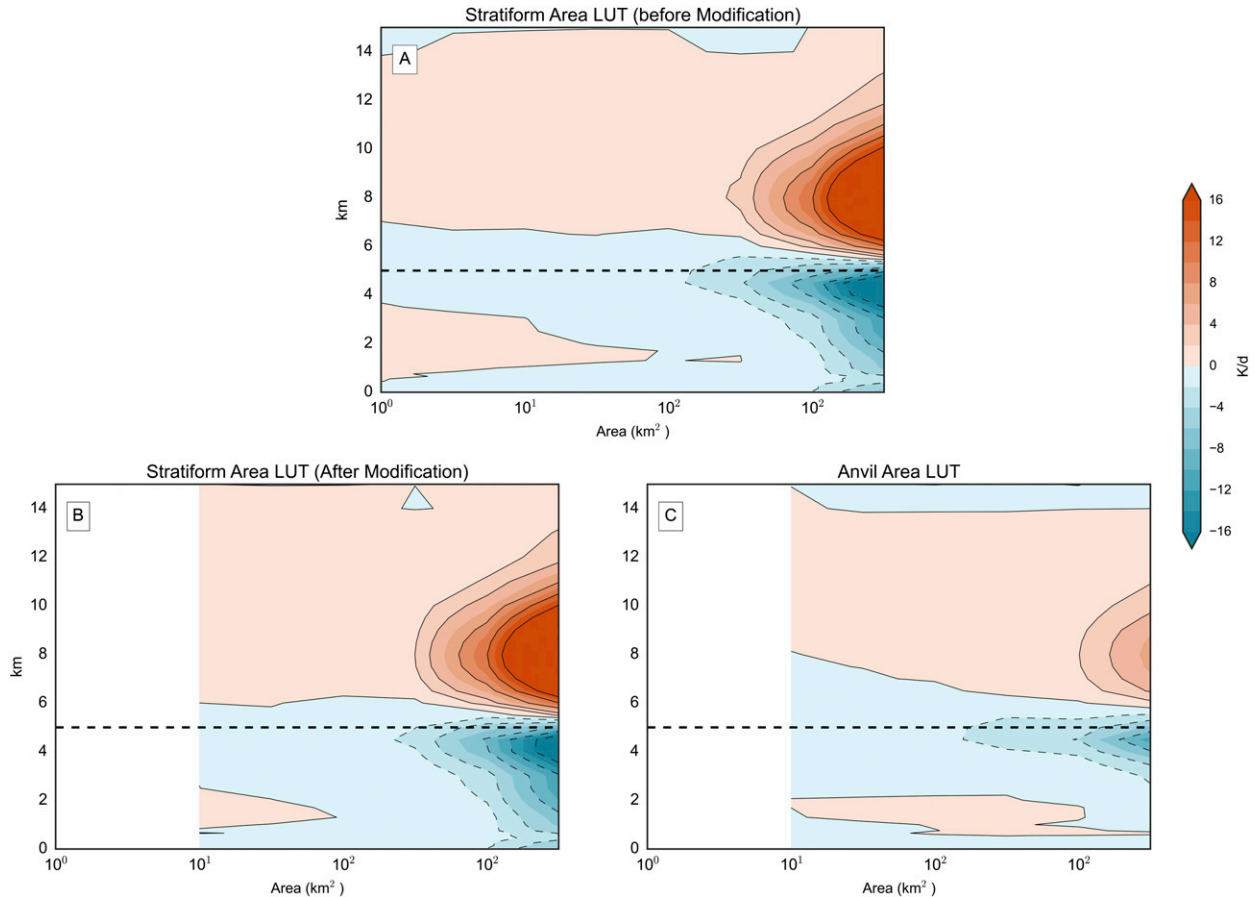


FIG. 6. (a) Stratiform LUT before modification, separated into (b) final stratiform LUT and (c) anvil LUT. The cluster area bins, which were chosen to adequately represent the cell population of all sizes, are logarithmically binned. Note that the latent heating values in each bin are averaged over the number of clusters and over the area of the model domain. The broken horizontal line indicates the climatological melting level at 5 km.

We now describe the construction of the heating retrieval algorithm, which is also illustrated in Fig. 5. After the WRF reflectivity is separated into convective and stratiform pixels and grouped into clusters, three echo characteristics are calculated for each cluster; namely, the echo area at the 2.5-km level, mean reflectivity at the 2.5-km level, and mean 10-dBZ echo-top height. Each cluster was then binned by these three parameters. The echo-top-height bins were spaced 1 km apart, extending from 0 to 14 km. The 2.5-km reflectivity bins ranged from 4 to 52 dBZ with a 4-dB interval. The bin sizes for the cluster areas were logarithmically spaced from 4 to 65 536 km² to accommodate a range of values spanning several orders of magnitude. The bin sizes were chosen to ensure that all the bins in the LUTs were statistically representative with at least 10 samples in each bin. If a particular bin did not contain at least 10 samples, it was merged with a neighbor in such a way that their combined number of samples summed up to at least 10. The merging process first happens across the intensity dimension and then the

echo-top-height dimension. The cluster area and echo-top heights can uniquely identify the cluster mean latent heating in most cases; the 2.5-km reflectivity is a proxy for the cluster rainfall intensity, distinguishing between dynamically active and decaying clusters of similar size and height. The latent heating profiles associated with all clusters in a given bin were averaged to have one representative heating profile per bin. The LUTs can then be applied to convective and stratiform clusters grouped from radar reflectivity data.

Upon examining the resultant LUTs, we found some unrealistic characteristics:

- Low-level stratiform heating—As already discussed, the model generally indicates low-level heating in regions of weak stratiform clusters (Figs. 4b,d) that is also evident in the stratiform LUT in Fig. 6a, especially at small cluster areas. However, these clusters almost certainly represent warm rain—convective processes in the tropics (Schumacher and Houze 2003) so a rain type

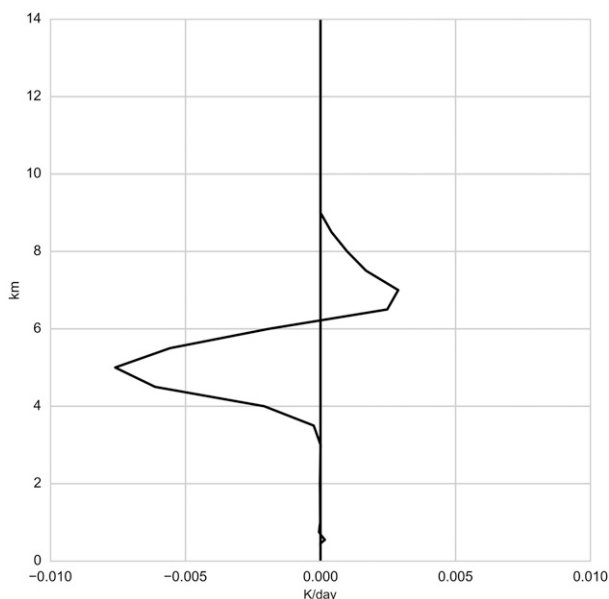


FIG. 7. Example anvil latent heating profile.

misclassification seems to be occurring. In addition, tropical stratiform precipitation is primarily found in MCSs (Rickenbach and Rutledge 1998; Xu and Rutledge 2015) and the MCS can be defined as having one horizontal dimension of at least 100 km in length (Houze 1997). Therefore, we expand upon the pixel-based Steiner et al. classification algorithm by using an area constraint, and we chose a conservative estimate of 200 km² as a threshold below which all stratiform clusters will be grouped under the convective category. The impact of the cutoff is shown in Fig. 6b, where most of the low-level heating is now absent. In addition, clusters that are sized close to the model's horizontal resolution could include numerical artifacts. Therefore, we neglect all clusters that are less than 4 km² in size in the convective LUT.

- Elevated profiles—Many of the stratiform rain clusters had latent heating profiles that transitioned from heating to cooling from 6 to 8 km, which is higher than expected based on the climatological height of the 0°C level of about 5 km over warm tropical oceans (Johnson et al. 1996). Stratiform cloud base is closely connected to the 0°C level (e.g., Leary and Houze 1979) such that cooling from sublimation above this level is unphysical in a region of stratiform rain. The WRF stratiform clusters with an elevated transition point also produced more cooling than warming in the column, with peak cooling greater than peak warming (e.g., Fig. 7). This is also unphysical in a raining cloud system since rain at the surface implies positive column-integrated latent heating [see Fig. 11 of Cifelli

and Rutledge (1998) for multiple examples of stratiform heating profiles from tropical field campaigns, all of which show greater warming in the column than cooling]. We termed these profiles anvil because the higher transition heights and net column cooling are more characteristic of nonprecipitating anvil clouds. In the construction of the stratiform LUTs, the clusters with a larger mean cooling peak than a warming peak but with a mean 2.5-km reflectivity less than 36 dBZ were classified as anvil (Fig. 6c). This removed most of the unphysical heating profiles from the modified stratiform LUT (Fig. 6b), but still retained the largest and most heavily raining clusters. When partitioned in this manner, the anvil category comprised 27% of all stratiform pixels in the model. Figure 6 shows that the latent heating contributed by the anvil clusters is weaker than the heating from equally sized stratiform clusters, particularly for the very largest clusters, where they are about 3 to 4 times weaker in magnitude. Another difference between the modified stratiform and anvil LUTs is the height of the transition from heating to cooling. The stratiform clusters have a consistent transition height near 6 km. In the case of the anvil clusters, the transition starts around 8 km for smaller clusters and approaches 6 km as the size of the clusters increase. This is indicative of the evolution of nonprecipitating anvil clouds, where the anvil cloud base descends and areal coverage increases with time (see Fig. 16 in Frederick and Schumacher 2008).

It is known that WRF (Hopper and Schumacher 2012) and other cloud-resolving models (May and Lane 2009) have issues with overestimating nonprecipitating anvil but it is unclear why the model creates these latent heating structures in rainy regions. Figure 8 shows the rainfall and number distribution for convective, stratiform, and anvil clusters. Anvil produces less rain than the stratiform rain clusters when separated by area, mean echo-top height, and mean 2.5-km reflectivity. However, the number of anvil clusters in the model is generally greater than the number of stratiform clusters, especially for smaller areas (<10³ km²) and small (<5 km) mean echo-top heights. This is consistent with the fact that anvil can form from both convective and stratiform rain regions and is not constrained by mesoscale processes and thus mesoscale spatial scales. The rain fractions for the stratiform and anvil components were 22.1% and 4.6%, respectively, giving a combined rain fraction of 26.7%. This is less than the observed tropics-wide average of 40% from TRMM observations (Schumacher and Houze 2003). However, underestimation of stratiform precipitation is a common bias in CRM and WRF simulations that is

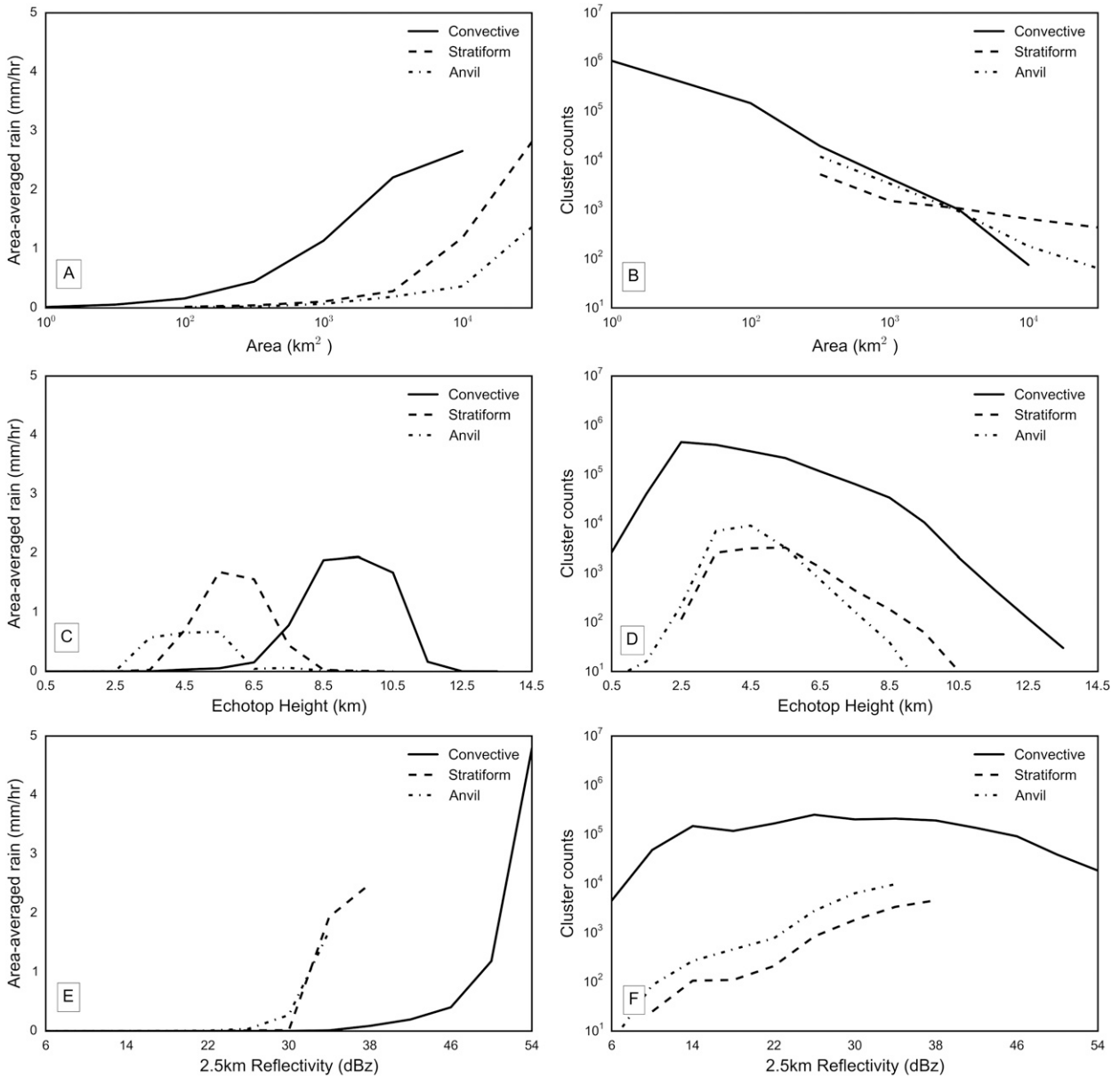


FIG. 8. The bin-averaged rain rate (mm h^{-1}) in convective, stratiform, and anvill LUTs vs (a) area, (c) 10-dBZ echo-top height, and (e) 2.5-km reflectivity. (b),(d),(f) As in (a), (c), and (e), but for the cluster distribution in each of the LUTs.

attributed to treatments in the microphysics parameterizations (Varble et al. 2011, 2014).

The modified stratiform and convective LUTs binned by average cluster reflectivity, cluster area, and mean cluster echo-top height are shown in Fig. 9 (the stratiform cluster area plot is repeated from Fig. 6b). Figures 9a and 9b show that latent heating in the stratiform and convective LUTs is predominantly restricted to a small range of mean reflectivity values, with stratiform cluster maximum heating and cooling centered around 34 dBZ and convective cell maximum

heating centered around 50 dBZ. Convective clusters with a mean 2.5-km reflectivity less than 32 dBZ have a distinctive region of cooling at midlevels and near the surface. The midlevel cooling is likely the result of detrainment driven evaporation and melting at cloud top in shallow convective and congestus clouds, while the near-surface cooling is likely a result of raindrop evaporation that creates cold pools (Feng et al. 2015). Figures 9c and 9d show that a larger area translates to a greater magnitude of heating for both stratiform and convective clusters, although the

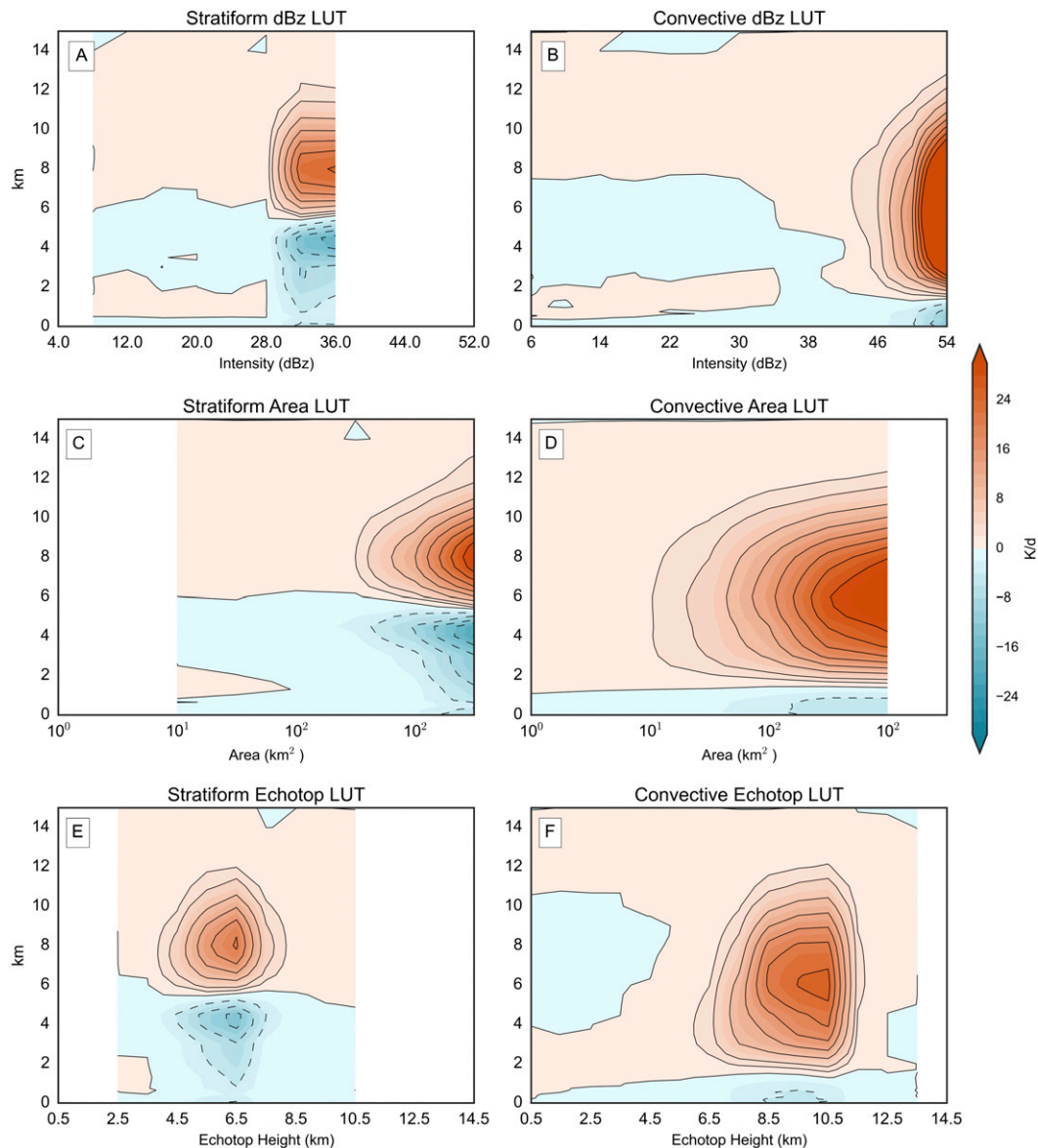


FIG. 9. The (left) stratiform and (right) convective modified LUTs with the heating (K day^{-1}) distributed by (a),(b) cluster reflectivity; (c),(d) cluster area; and (e),(f) mean cluster 10-dBZ echo-top height. The heating is normalized by the number of clusters in each category.

convective cluster area does not exceed the $16\,384\text{ km}^2$ bin. Figures 9e and 9f show how the latent heating is partitioned by the mean cluster 10-dBZ echo-top height. For stratiform rain, the greater part of the latent heating is contained in clusters with mean 10-dBZ echo-top heights between 5 and 7 km. The radar simulator built into WRF accounts for precipitating hydrometeors, but neglects cloud water and cloud ice (see section 3.2 in Hagos et al. 2014). The occurrence of heating above the 10-dBZ echo-top height is therefore possibly attributed to the presence of small hydrometeors that are invisible at S band (10-cm

wavelength). Nevertheless, 10 dBZ was retained as the threshold for cell height because most scanning centimeter-wavelength radars are not fully sensitive below this threshold at distance (e.g., 150 km) from the radar. The convective clusters show a deepening heating mode with increasing mean echo-top height. There is a heating maximum at 4 km for clusters with mean echo tops around 6 km, and a deeper maximum centered at 6 km for mean echo tops greater than 8 km. This latter result is consistent with the fact that deep convective tropical heating is usually assumed to peak in the midtroposphere ($\sim 6\text{ km}$; Houze 1982,

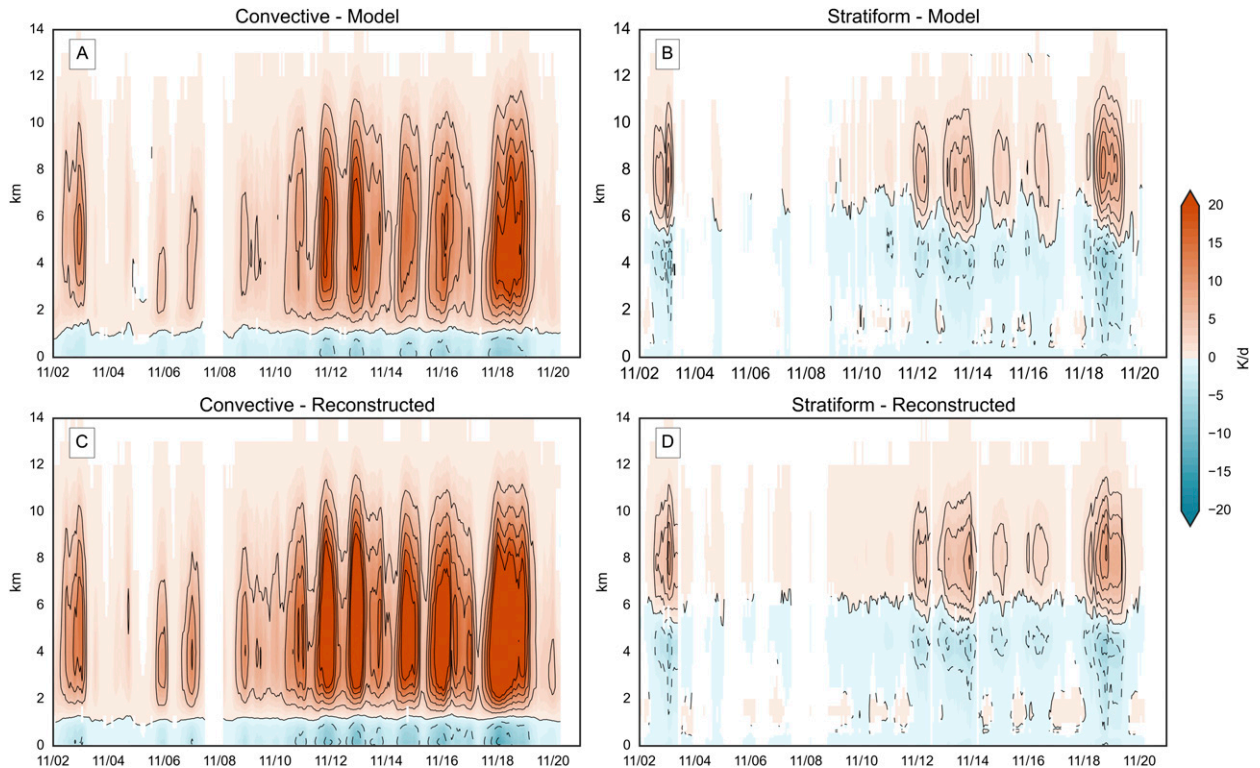


FIG. 10. For November 2011, (a) convective and (b) stratiform model latent heating, along with (c) convective and (d) stratiform latent heating reconstructed using the CSA algorithm. The latent heating values (K day^{-1}) are hourly values averaged over the entire model domain.

1989). Figure 9f shows that the detrainment cooling at cloud top is restricted to shallow clusters having mean 10-dBZ echo-top heights less than 5 km. This result is consistent with the Q_1 profiles for congestus clouds observed during the Kwajalein Experiment (Schumacher et al. 2008).

Figure 10 compares the latent heating that is produced directly from the model microphysics scheme with the reconstructed heating from the LUTs in Fig. 9 for 20 days in November 2011 during DYNAMO for convective and stratiform rain regions. We hereinafter refer to this LUT method as the convective–stratiform area (CSA) algorithm. CSA is able to accurately reconstruct the latent heating time series, capturing all the variations including the inactive period early in the month, the buildup in shallow convection in the middle of the month, and the burst of deep convective and stratiform heating in the latter half of the time series. The mean convective and stratiform latent heating profiles for the model and CSA reconstruction are also consistent (not shown). We performed a test for robustness by reconstructing the first half of the time series using a LUT constructed from the second half and the LUT was able to satisfactorily reproduce the model heating (not shown).

4. Application to S-PolKa observations

It is important to preface this section with a note on the convergence problem of model physics, as identified in Arakawa (2004) and Jung and Arakawa (2004). In these studies, the authors pointed out that no amount of time and space averaging can make the heating profiles from high-resolution models converge with those of the low-resolution models because of the effect of subgrid-scale transport terms. A characteristic of CRM-derived stratiform heating profiles is sharp heating and cooling peaks, along with a sharp transition from heating to cooling [see Figs. 5b and 10 in Shige et al. (2004) and Fig. 9 in Skyllingstad and De Szoek (2015)]. This is in contrast to the smooth heating profiles from “low resolution” heating budgets (Stachnik et al. 2013). Therefore, we would not expect an exact match between the CRM profiles and observed large-scale budget studies.

The CSA algorithm was applied to the observed radar reflectivity from the range–height indicator (RHI) sector scans from S-PolKa for 2 October to 30 December 2011. The RHI scans were executed from an elevation angle of 0.5° to 40° at an azimuthal increment of 0.5° . The RHI sector is shown in Fig. 1 of Hagos et al. (2014) and was chosen over the surveillance scans (with 11° maximum

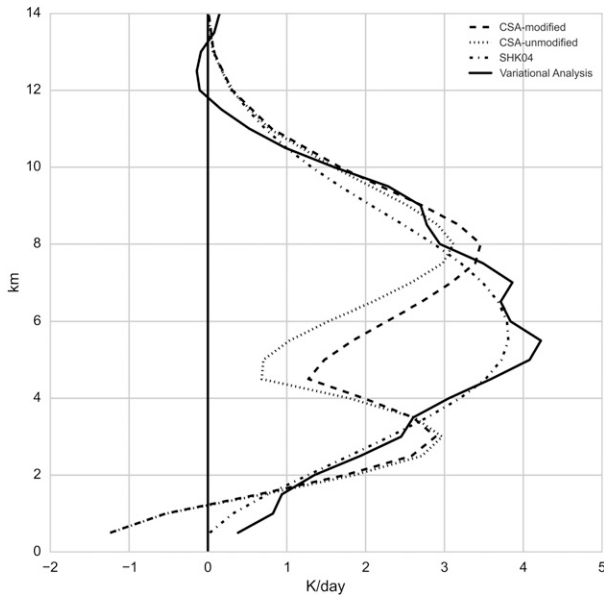


FIG. 11. S-PolKa-derived latent heating (K day^{-1}) profiles from 2 Oct to 30 Dec 2011. The variational analysis heating profile represents Q_1 from the reanalysis and sounding budget over the S-PolKa area.

elevation) because of greater vertical coverage close to the radar. The heating from the CSA algorithm was then compared with two other latent heating retrievals, one based on the idealized profiles from Schumacher et al. (2004) described in the introduction (hereinafter, SHK04) and the other, the Q_1 sounding budget method described in section 2.

Figure 11 shows the average latent heating profile for the 3-month period for each method and includes CSA profiles with (CSA unmodified) and without (CSA modified) anvil included in the stratiform LUT. The SHK04 and Q_1 profiles are consistent, in part because the overall magnitude of heating is expected to agree between these two methods given that both techniques are constrained using the same S-PolKa estimated surface rainfall. However, the distribution of heating in the vertical is determined independently. The CSA latent heating profiles have a double heating peak at 3.5 and 8 km in contrast to a single heating peak found in the Q_1 profile at 5.5 km. The magnitude of the CSA-unmodified peak is $\sim 3 \text{ K day}^{-1}$, as compared with the variational analysis peak of $\sim 4 \text{ K day}^{-1}$. Excluding the anvil-like stratiform clusters (CSA modified) increases the heating magnitude at mid- and upper levels, but the mean latent heating profile still retains a distinct minimum at midlevels, which is indicative of strong stratiform cooling in the model. The modified CSA heating profile shows a stronger upper-level heating peak of comparable magnitude (3.5 K day^{-1}) to the variational analysis, albeit at a higher elevation (7 km) potentially indicative of a larger stratiform component. A low-level heating peak of $\sim 3 \text{ K day}^{-1}$ is observed near the 3-km level, which is a signature of the bottom-heavy convective heating. The SHK04 profile does not show a sharp cooling at midlevels because it uses smooth, idealized input profiles.

Figure 12 separates the convective and stratiform components of the SHK04 and CSA latent heating

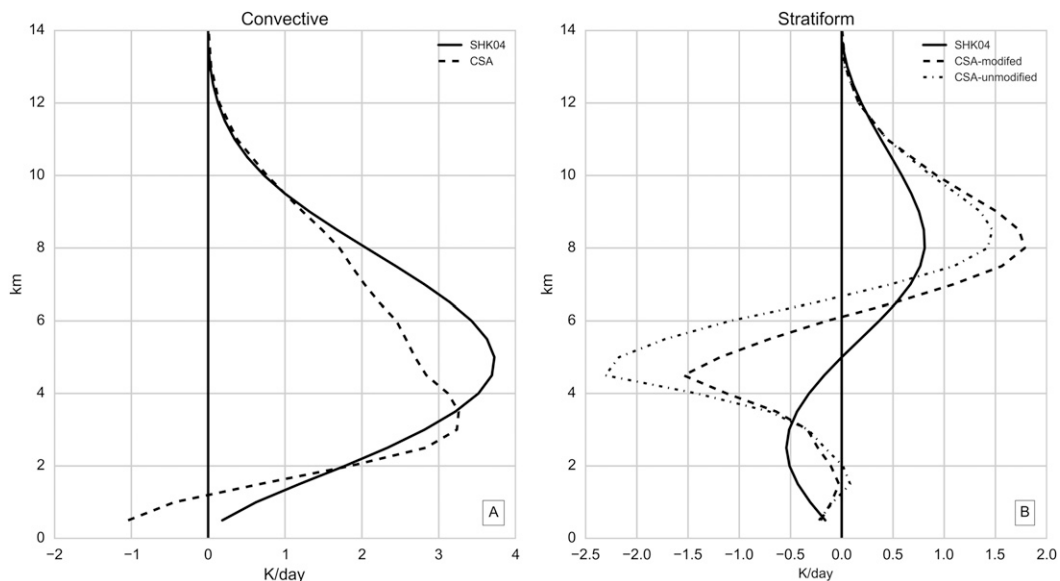


FIG. 12. S-PolKa-derived latent heating (K day^{-1}) profiles from 2 Oct to 30 Dec 2011 for (a) convective and (b) stratiform rain regions.

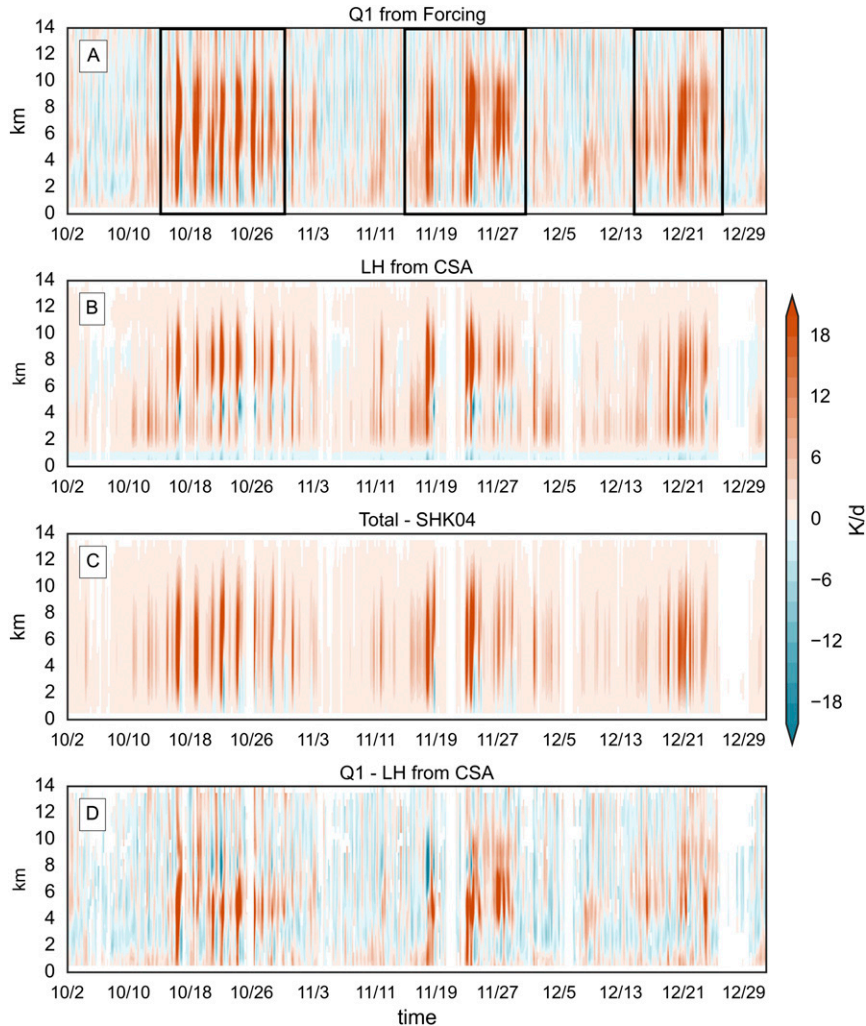


FIG. 13. Time series from 2 Oct to 30 Dec 2011 for (a) Q_1 from the forcing dataset, (b) S-PolKa latent heating from CSA, (c) S-PolKa latent heating from the SHK04 algorithm, and (d) the difference between Q_1 and CSA-derived latent heating. White areas indicate times when the heating was between $\pm 10^{-3}$ K, which includes days when S-Pol was not in operation. Black rectangles in (a) indicate active phases of the MJO.

profiles from Fig. 11. There is good correspondence between the magnitudes of the convective heating profiles (Fig. 12a), even though the CRM-based convective heating is more bottom heavy than the idealized heating profile from SHK04. Clear differences exist in the stratiform profiles (Fig. 12b). The transition from lower-level cooling to upper-level heating occurs at 5 km in SHK04 as compared with 6.5 km in the uncorrected CSA. The magnitudes of the uncorrected heating and cooling peaks are larger when compared with SHK04 (-2.2 vs -0.5 K day $^{-1}$), giving net cooling in the column despite the presence of surface rain. This feature, as discussed in section 3, is unphysical, and the exclusion of the anvil heating from the LUT results in an average heating profile with a lower transition level

(~ 6 km). The heating peak in the corrected stratiform profile is also larger than the idealized heating of SHK04 (1.7 K vs 0.5 K day $^{-1}$). This increase in the stratiform heating makes the overall heating profile more top heavy. However, the altitude of the cooling peak in the corrected stratiform heating remains near 4 km, suggesting that cooling from melting near the 0°C level is a dominant process in the model.

Figure 13 depicts the S-PolKa latent heating time series from 2 October to 30 December 2011 for the variational analysis Q_1 , CSA, and SHK04 methods. The three MJO active phases are seen in the heating signatures for October (15–27), November (16–29), and December (16–26) and are indicated by black boxes. Each event shows a rise in the heating peak, typifying

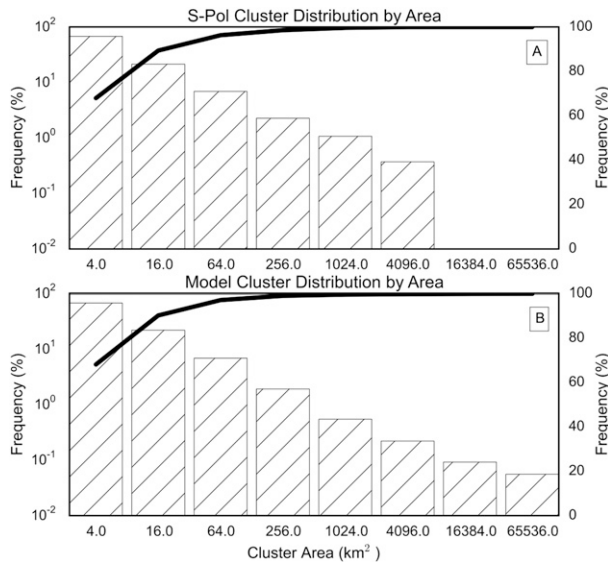


FIG. 14. (top) S-PolKa and (bottom) model stratiform clusters distributed by area from 2 Oct to 30 Dec 2011. The left y axis is logarithmic and shows the stratiform cluster distribution. The dark line is the cumulative distribution function and is shown using the linear y axis, on the right.

the westward tilt in heating associated with the MJO (Kiladis et al. 2005, Benedict and Randall 2007), followed by a quiescent period. Each method captures the temporal variations in convective activity during this time period. The transition from shallow to deep heating is clearly captured by the CSA method in the altitude of peak heating (Fig. 13b); however, the SHK04 heating profiles do not vary as much in height in the buildup to the active MJO because it only assumes two possible convective heating profiles (Fig. 13c). SHK04 also shows much less variation in low-level cooling than does the CSA method because of its single stratiform profile that has no sensitivity to variations in the mesoscale downdraft and evaporation below cloud base. Another advantage of using the CSA over the SHK04 is that the former can capture the transition in time of the convective and stratiform peak heating. The accurate representation of this temporal variability of the shape of the heating could be fundamental to MJO simulations (Lin et al. 2004) and its theoretical description (Mapes 2000). The CSA method also captures the top-heaviness of the heating profiles better than the SHK04 technique during the periods of active MJO (indicated by black boxes in Fig. 13a). However, an examination of the mean heating profiles in Fig. 11 suggests that the CSA might be exaggerating the magnitude of midlevel cooling.

The difference between the Q_1 and the CSA-derived latent heating (Fig. 13d) shows the temporal variation of

differences seen in Fig. 11. The cooling due to evaporation near the boundary layer is captured in the CSA method, but is not visible in Q_1 . The quantity Q_1 also produces greater values of heating at midlevels during the active MJO, which can be traced to the strong cooling seen in CSA's stratiform profiles. During the convectively quiescent times, Q_1 is likely to be dominated by longwave cooling that is not included in the CSA retrieval. The CSA algorithm is able to reproduce a realistic time series of latent heating without any rain rate information. Since radar-derived surface rain was used to constrain the forcing dataset, the CSA heating profiles represent a less-derived product that is directly obtained from the radar reflectivity data and information about the organization of the convective system.

Since the CSA LUT was created using a region that was much larger than the S-PolKa domain (Fig. 1), it could have a cluster distribution much different from what is seen by the radar. Figure 14 compares the histogram of S-PolKa stratiform cluster area distribution from 2 October to 30 December with that of the model for 1–20 November. All of the clusters are on the order of 10^3 km², whereas the model stratiform LUT in Fig. 9 extends to 10^4 km². To assess whether the scale mismatch between the model and radar domains would affect the CSA performance, we created another LUT that only considered precipitating echoes within a model region similar to the size of the S-PolKa 150-km radius domain (the dark gray area in Fig. 1). This radar domain-sized LUT was also made statistically representative by imposing the condition of including at least 10 samples per bin. Figure 15 compares the convective and stratiform heating profiles from the full and truncated model domain LUTs. There is little change in the convective heating profiles, but the stratiform cooling and heating peaks diminish in magnitude by about 0.3 and 0.5 K day⁻¹, respectively. This decrease in magnitude is most likely due to the fact that the largest stratiform clusters (which produce the largest heating and cooling, as seen in Fig. 9c) are too large for a typical ground-radar domain to capture. The time series of latent heating from the radar-sized domain also corresponds well with that from the full model domain (not shown).

5. Conclusions

We present a new technique to retrieve latent heating profiles from ground-based or spaceborne radar-observed precipitating echo characteristics (i.e., size, mean echo-top height, and mean low-level reflectivity) rather than derived rainfall information. Contiguous regions of convective and stratiform rain are grouped to form clusters, which are then assigned heating profiles based on output

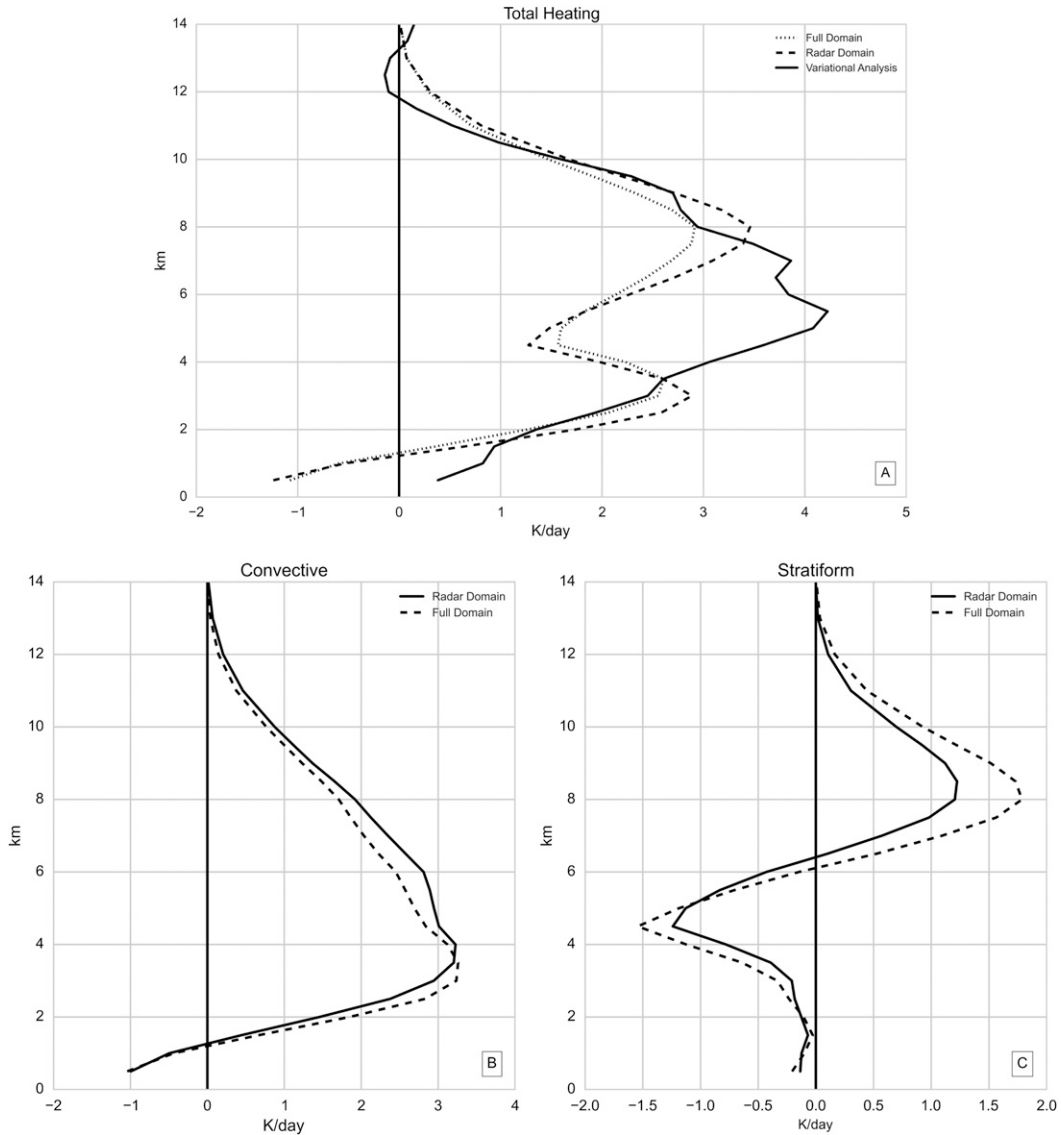


FIG. 15. S-PolKa latent heating profiles ($K\ day^{-1}$) from the radar-scale domain and the full model domain for (a) total, (b) convective, and (c) stratiform rain regions using the CSA algorithm. The Q_1 profile from the variational analysis is included in (a).

from a 500-m regional WRF simulation during the DYNAMO/CINDY2011/AMIE field campaign. We decided on the 500-m run over the 2-km run after we found that it improved upon the pervasive low-level heating peak in the convective and stratiform heating profiles. Reclassifying regions smaller than $200\ km^2$ as convective also reduced the incidence of the low-level heating peak in stratiform profiles.

The model clusters were sorted according to area at 2.5 km, mean 10-dBZ echo-top height, and the average reflectivity at 2.5 km to create a set of lookup tables. The original stratiform LUT included heating profiles that showed transition from heating to cooling well above the

$0^\circ C$ level that led to net column cooling (unphysical when rain is present). The anvil-like heating profiles with weak rain near the surface were removed from the stratiform LUT to mitigate some of these issues. The first issue is most likely due to an error in the convective–stratiform separation technique, but both issues potentially highlight problems in the model resolution as well as PBL and microphysics parameterizations.

The CSA LUTs were applied to S-PolKa reflectivity observations and the resulting latent heating profiles were generally consistent with the Q_1 from variational analysis and the latent heating retrieval from S-PolKa using the simpler SHK04 method, including capturing

realistic temporal variations associated with the evolution of the MJO. However, the CSA stratiform LUT produced much larger cooling near the melting level, as would be expected based on arguments made in Arakawa (2004). A sensitivity test showed that the CSA technique can be applied across scales ranging from a relatively small radar domain to a larger model domain in the near-equatorial Indian Ocean to produce quantitatively similar results.

Future algorithm development will include further investigation into the cause of the anomalous low-level heating spike in the WRF stratiform profiles and the anvil-like net cooling in regions of stratiform rain. We also plan to assess the robustness of the technique using LUTs from other tropical oceanic and land field campaigns. Since we expect the heating properties of the clusters themselves to be unchanging over different seasons with only their frequency varying, we expect the LUTs generated for one season to be valid in another, at least over tropical oceans. In other regimes, such as land or monsoonal regions, a model that can satisfactorily capture the convective variation in those regimes will have to be run again, to generate the LUT. Any biases in those models will be addressed on a case-by-case basis. We are optimistic about the application of the CSA in higher latitudes [e.g., for NASA's Global Precipitation Measurement (GPM) program] where a heating retrieval based on the size and organization of a system may be more robust and physically realistic than pixel, rain-based estimates. This is because midlatitude convection, though forced by different large-scale dynamics than tropical convection, is still often organized into mesoscale convective systems (Maddox 1980; Parker and Johnson 2000), with distinct heating structures for convective and stratiform components.

Acknowledgments. The DYNAMO field campaign data used in this paper are available at NCAR's Earth Observing Laboratory's DYNAMO Data Catalogue https://www.eol.ucar.edu/field_projects/dynamo. The dataset names are S-PolKa Radar, fully corrected, merged, final moments data in cfRadial format. This research was supported by NSF Grant AGS-1062217 and DOE Grant DE-SC0000798 to Texas A&M University. It is also based on work supported by the Biological and Environmental Research of the DOE Office of Science as part of the Regional and Global Climate Modeling Program and Atmospheric System Research Program. Computing resources for the simulations were provided by the National Energy Research Scientific Computing Center (NERSC). The Pacific Northwest National Laboratory is operated for DOE by Battelle Memorial Institute under Contract

DE-AC05-76RL01830. The authors thank the three anonymous reviewers whose observations and suggestions lent lucidity and greatly improved the quality of this work.

REFERENCES

- Arakawa, A., 2004: The cumulus parameterization problem: Past, present, and future. *J. Climate*, **17**, 2493–2525, doi:10.1175/1520-0442(2004)017<2493:RATCPP>2.0.CO;2.
- Austin, P. M., 1987: Relation between measured radar reflectivity and surface rainfall. *Mon. Wea. Rev.*, **115**, 1053–1070, doi:10.1175/1520-0493(1987)115<1053:RBMRRR>2.0.CO;2.
- Benedict, J. J., and D. A. Randall, 2007: Observed characteristics of the MJO relative to maximum rainfall. *J. Atmos. Sci.*, **64**, 2332–2354, doi:10.1175/JAS3968.1.
- Brown, J. M., 1979: Mesoscale unsaturated downdrafts driven by rainfall evaporation: A numerical study. *J. Atmos. Sci.*, **36**, 313–338, doi:10.1175/1520-0469(1979)036<0313:MUDDBR>2.0.CO;2.
- Bryan, G. H., and H. Morrison, 2012: Sensitivity of a simulated squall line to horizontal resolution and parameterization of microphysics. *Mon. Wea. Rev.*, **140**, 202–225, doi:10.1175/MWR-D-11-00046.1.
- Chan, S. C., and S. Nigam, 2009: Residual diagnosis of diabatic heating from ERA-40 and NCEP reanalyses: Intercomparisons with TRMM. *J. Climate*, **22**, 414–442, doi:10.1175/2008JCLI2417.1.
- Chen, T.-C., and M.-C. Yen, 1991: A study of the diabatic heating associated with the Madden-Julian oscillation. *J. Geophys. Res.*, **96**, 13 163–13 177, doi:10.1029/91JD01356.
- Cifelli, R., and S. A. Rutledge, 1998: Vertical motion, diabatic heating, and rainfall characteristics in north Australia convective systems. *Quart. J. Roy. Meteor. Soc.*, **124**, 1133–1162, doi:10.1002/qj.49712454806.
- Dudhia, J., 1989: Numerical study of convection observed during the Winter Monsoon Experiment using a mesoscale two-dimensional model. *J. Atmos. Sci.*, **46**, 3077–3107, doi:10.1175/1520-0469(1989)046<3077:NSOCOD>2.0.CO;2.
- Feng, Z., S. Hagos, A. K. Rowe, C. D. Burleyson, M. N. Martini, and S. P. de Szoeke, 2015: Mechanisms of convective cloud organization by cold pools over tropical warm ocean during the AMIE/DYNAMO field campaign. *J. Adv. Model. Earth Syst.*, **7**, 357–381, doi:10.1002/2014MS000384.
- Frederick, K., and C. Schumacher, 2008: Anvil characteristics as seen by C-POL during the Tropical Warm Pool International Cloud Experiment (TWP-ICE). *Mon. Wea. Rev.*, **136**, 206–222, doi:10.1175/2007MWR2068.1.
- Gill, A. E., 1980: Some simple solutions for heat-induced tropical circulation. *Quart. J. Roy. Meteor. Soc.*, **106**, 447–462, doi:10.1002/qj.49710644905.
- Greco, M., and S. W. Olson, 2006: Bayesian estimation of precipitation from satellite passive microwave observations using combined radar–radiometer retrievals. *J. Appl. Meteor. Climatol.*, **45**, 416–433, doi:10.1175/JAM2360.1.
- Hagos, S., 2010: Building blocks of tropical diabatic heating. *J. Atmos. Sci.*, **67**, 2341–2354, doi:10.1175/2010JAS3252.1.
- , and C. Zhang, 2010: Diabatic heating, divergent circulation and moisture transport in the African monsoon system. *Quart. J. Roy. Meteor. Soc.*, **136**, 411–425, doi:10.1002/qj.538.
- , and L. R. Leung, 2011: Moist thermodynamics of the Madden-Julian oscillation in a cloud-resolving simulation. *J. Climate*, **24**, 5571–5583, doi:10.1175/2011JCLI4212.1.

- , and Coauthors, 2010: Estimates of tropical diabatic heating profiles: Commonalities and uncertainties. *J. Climate*, **23**, 542–558, doi:10.1175/2009JCLI3025.1.
- , Z. Feng, C. D. Burleyson, K.-S. S. Lim, C. N. Long, D. Wu, and G. Thompson, 2014: Evaluation of convection-permitting model simulations of cloud populations associated with the Madden-Julian oscillation using data collected during the AMIE/DYNAMO field campaign. *J. Geophys. Res. Atmos.*, **119**, 12 052–12 068, doi:10.1002/2014JD022143.
- Hartmann, D. L., H. H. Hendon, and R. A. Houze Jr., 1984: Some implications of the mesoscale circulations in tropical cloud clusters for large-scale dynamics and climate. *J. Atmos. Sci.*, **41**, 113–121, doi:10.1175/1520-0469(1984)041<0113:SIOTMC>2.0.CO;2.
- Hopper, L. J., and C. Schumacher, 2012: Modeled and observed variations in storm divergence and stratiform rain production in southeastern Texas. *J. Atmos. Sci.*, **69**, 1159–1181, doi:10.1175/JAS-D-11-092.1.
- Houze, R. A., Jr., 1982: Cloud clusters and large-scale vertical motions in the tropics. *J. Meteor. Soc. Japan*, **60**, 396–410.
- , 1989: Observed structure of mesoscale convective systems and implications for large-scale heating. *Quart. J. Roy. Meteor. Soc.*, **115**, 425–461, doi:10.1002/qj.49711548702.
- , 1997: Stratiform precipitation in regions of convection: A meteorological paradox? *Bull. Amer. Meteor. Soc.*, **78**, 2179–2196, doi:10.1175/1520-0477(1997)078<2179:SPIROC>2.0.CO;2.
- , and A. K. Betts, 1981: Convection in GATE. *Rev. Geophys.*, **19**, 541–576, doi:10.1029/RG019i004p00541.
- , S. Brodzik, C. Schumacher, S. E. Yuter, and C. R. Williams, 2004: Uncertainties in oceanic radar rain maps at Kwajalein and implications for satellite validation. *J. Appl. Meteor.*, **43**, 1114–1132, doi:10.1175/1520-0450(2004)043<1114:UIORRM>2.0.CO;2.
- Iacono, M. J., E. J. Mlawer, S. A. Clough, and J.-J. Morcrette, 2000: Impact of an improved longwave radiation model, RRTM, on the energy budget and thermodynamic properties of the NCAR Community Climate Model, CCM3. *J. Geophys. Res.*, **105**, 14 873–14 890, doi:10.1029/2000JD900091.
- Janjić, Z. I., 2001: Nonsingular implementation of the Mellor–Yamada level 2.5 scheme in the NCEP Meso Model, NOAA/NWS/ NCEP Office Note 437, 61 pp. [Available online at <http://www.emc.ncep.noaa.gov/officenotes/newernotes/on437.pdf>.]
- Jiang, X., and Coauthors, 2011: Vertical diabatic heating structure of the MJO: Intercomparison between recent reanalyses and TRMM estimates. *Mon. Wea. Rev.*, **139**, 3208–3223, doi:10.1175/2011MWR3636.1.
- Jin, Q., X.-Q. Yang, X.-G. Sun, and J.-B. Fang, 2013: East Asian summer monsoon circulation structure controlled by feedback of condensational heating. *Climate Dyn.*, **41**, 1885–1897, doi:10.1007/s00382-012-1620-9.
- Johnson, R. H., and G. S. Young, 1983: Heat and moisture budgets of tropical mesoscale anvil clouds. *J. Atmos. Sci.*, **40**, 2138–2147, doi:10.1175/1520-0469(1983)040<2138:HAMBOT>2.0.CO;2.
- , P. E. Ciesielski, and K. A. Hart, 1996: Tropical inversions near the 0°C level. *J. Atmos. Sci.*, **53**, 1838–1855, doi:10.1175/1520-0469(1996)053<1838:TINTL>2.0.CO;2.
- Jung, J. H., and A. Arakawa, 2004: The resolution dependence of model physics: Illustrations from nonhydrostatic model experiments. *J. Atmos. Sci.*, **61**, 88–102, doi:10.1175/1520-0469(2004)061<0088:TRDOMP>2.0.CO;2.
- Kiladis, G. N., K. H. Straub, and P. T. Haertel, 2005: Zonal and vertical structure of the Madden–Julian oscillation. *J. Atmos. Sci.*, **62**, 2790–2809, doi:10.1175/JAS3520.1.
- Lac, C., and J. P. Lafore, 2002: Role of gravity waves in triggering deep convection during TOGA COARE. *J. Atmos. Sci.*, **59**, 1293–1316, doi:10.1175/1520-0469(2002)059<1293:ROGWIT>2.0.CO;2.
- Lappen, C.-L., and C. Schumacher, 2012: Heating in the tropical atmosphere: What level of detail is critical for accurate MJO simulations in GCMs? *Climate Dyn.*, **39** (9–10), 2547–2568, doi:10.1007/s00382-012-1327-y.
- Leary, C. A., and R. A. Houze Jr., 1979: Melting and evaporation of hydrometeors in precipitation from the anvil clouds of deep tropical convection. *J. Atmos. Sci.*, **36**, 669–679, doi:10.1175/1520-0469(1979)036<0669:MAEOHI>2.0.CO;2.
- Li, C., X. Jia, J. Ling, W. Zhou, and C. Zhang, 2009: Sensitivity of MJO simulations to diabatic heating profiles. *Climate Dyn.*, **32** (2–3), 167–187, doi:10.1007/s00382-008-0455-x.
- Lin, J. L., B. Mapes, M. H. Zhang, and M. Newman, 2004: Stratiform precipitation, vertical heating profiles, and the Madden–Julian oscillation. *J. Atmos. Sci.*, **61**, 296–309, doi:10.1175/1520-0469(2004)061<0296:SPVHPA>2.0.CO;2.
- Ling, J., and C. Zhang, 2011: Structural evolution in heating profiles of the MJO in global reanalyses and TRMM retrievals. *J. Climate*, **24**, 825–842, doi:10.1175/2010JCLI3826.1.
- Maddox, R. A., 1980: Mesoscale convective complexes. *Bull. Amer. Meteor. Soc.*, **61**, 1374–1387, doi:10.1175/1520-0477(1980)061<1374:MCC>2.0.CO;2.
- Mapes, B. E., 1993: Gregarious tropical convection. *J. Atmos. Sci.*, **50**, 2026–2037, doi:10.1175/1520-0469(1993)050<2026:GTC>2.0.CO;2.
- , 2000: Convective inhibition, subgrid-scale triggering energy, and stratiform instability in a toy tropical wave model. *J. Atmos. Sci.*, **57**, 1515–1535, doi:10.1175/1520-0469(2000)057<1515:CISSTE>2.0.CO;2.
- , and R. A. Houze, 1995: Diabatic divergence profiles in western Pacific mesoscale convective systems. *J. Atmos. Sci.*, **52**, 1807–1828, doi:10.1175/1520-0469(1995)052<1807:DDPIWP>2.0.CO;2.
- , P. E. Ciesielski, and R. H. Johnson, 2003: Sampling errors in rawinsonde-array budgets. *J. Atmos. Sci.*, **60**, 2697–2714, doi:10.1175/1520-0469(2003)060<2697:SEIRB>2.0.CO;2.
- May, P. T., and T. P. Lane, 2009: A method for using weather radar data to test cloud resolving models. *Meteor. Appl.*, **16**, 425–432, doi:10.1002/met.150.
- Olson, W. S., C. D. Kummerow, Y. Hong, and W. K. Tao, 1999: Atmospheric latent heating distributions in the tropics derived from satellite passive microwave radiometer measurements. *J. Appl. Meteor.*, **38**, 633–664, doi:10.1175/1520-0450(1999)038<0633:ALHDIT>2.0.CO;2.
- , and Coauthors, 2006: Precipitation and latent heating distributions from satellite passive microwave radiometry. Part I: Improved method and uncertainties. *J. Appl. Meteor. Climatol.*, **45**, 702–720, doi:10.1175/JAM2369.1.
- Parker, M. D., and R. H. Johnson, 2000: Organizational modes of midlatitude mesoscale convective systems. *Mon. Wea. Rev.*, **128**, 3413–3436, doi:10.1175/1520-0493(2001)129<3413:OMOMMC>2.0.CO;2.
- Rickenbach, T. M., and S. A. Rutledge, 1998: Convection in TOGA COARE: Horizontal scale, morphology, and rainfall production. *J. Atmos. Sci.*, **55**, 2715–2729, doi:10.1175/1520-0469(1998)055<2715:CITCHS>2.0.CO;2.
- Schumacher, C., and R. A. Houze Jr., 2003: The TRMM Precipitation Radar’s view of shallow, isolated rain. *J. Appl. Meteor.*, **42**, 1519–1524, doi:10.1175/1520-0450(2003)042<1519:TTPRVO>2.0.CO;2.

- , —, and I. Kraucunas, 2004: The tropical dynamical response to latent heating estimates derived from the TRMM Precipitation Radar. *J. Atmos. Sci.*, **61**, 1341–1358, doi:10.1175/1520-0469(2004)061<1341:TTDRTL>2.0.CO;2.
- , M. H. Zhang, and P. E. Ciesielski, 2007: Heating structures of the TRMM field campaigns. *J. Atmos. Sci.*, **64**, 2593–2610, doi:10.1175/JAS3938.1.
- , P. E. Ciesielski, and M. H. Zhang, 2008: Tropical cloud heating profiles: Analysis from KWAJEX. *Mon. Wea. Rev.*, **136**, 4289–4300, doi:10.1175/2008MWR2275.1.
- Shige, S., Y. N. Takayabu, W.-K. Tao, and D. E. Johnson, 2004: Spectral retrieval of latent heating profiles from TRMM PR data. Part I: Development of a model-based algorithm. *J. Appl. Meteor.*, **43**, 1095–1113, doi:10.1175/1520-0450(2004)043<1095:SR0LHP>2.0.CO;2.
- Skyllingstad, E. D., and S. P. de Szoeke, 2015: Cloud-resolving large-eddy simulation of tropical convective development and surface fluxes. *Mon. Wea. Rev.*, **143**, 2441–2458, doi:10.1175/MWR-D-14-00247.1.
- Smith, P. L., 1984: Equivalent radar reflectivity factors for snow and ice particles. *J. Appl. Meteor.*, **23**, 1258–1260, doi:10.1175/1520-0450(1984)023<1258:ERRFFS>2.0.CO;2.
- Stachnik, J. P., C. Schumacher, and P. E. Ciesielski, 2013: Total heating characteristics of the ISCCP tropical and subtropical cloud regimes. *J. Climate*, **26**, 7097–7116, doi:10.1175/JCLI-D-12-00673.1.
- Steiner, M., R. A. Houze Jr., and S. E. Yuter, 1995: Climatological characterization of three-dimensional storm structure from operational radar and rain gauge data. *J. Appl. Meteor.*, **34**, 1978–2007, doi:10.1175/1520-0450(1995)034<1978:CCOTDS>2.0.CO;2.
- Stoelinga, M. T., 1996: A potential vorticity-based study of the role of diabatic heating and friction in a numerically simulated baroclinic cyclone. *Mon. Wea. Rev.*, **124**, 849–874, doi:10.1175/1520-0493(1996)124<0849:APVBSO>2.0.CO;2.
- Tao, W.-K., and J. Simpson, 1989: Modeling study of a tropical squall-type convective line. *J. Atmos. Sci.*, **46**, 177–202, doi:10.1175/1520-0469(1989)046<0177:M0ATS>2.0.CO;2.
- , S. Lang, J. Simpson, and R. Adler, 1993a: Retrieval algorithms for estimating the vertical profiles of latent heat release—Their applications for TRMM. *J. Meteor. Soc. Japan*, **71**, 685–700.
- , J. Simpson, C. H. Sui, B. Ferrier, S. Lang, J. Scala, M. D. Chou, and K. Pickering, 1993b: Heating, moisture, and water budgets of tropical and midlatitude squall lines: Comparisons and sensitivity to longwave radiation. *J. Atmos. Sci.*, **50**, 673–690, doi:10.1175/1520-0469(1993)050<0673:HMAWBO>2.0.CO;2.
- , and Coauthors, 2006: Retrieval of latent heating from TRMM measurements. *Bull. Amer. Meteor. Soc.*, **87**, 1555–1572, doi:10.1175/BAMS-87-11-1555.
- , S. Lang, X. Zeng, S. Shige, and Y. Takayabu, 2010: Relating convective and stratiform rain to latent heating. *J. Climate*, **23**, 1874–1893, doi:10.1175/2009JCLI3278.1.
- Thompson, G., P. R. Field, R. M. Rasmussen, and W. D. Hall, 2008: Explicit forecasts of winter precipitation using an improved bulk microphysics scheme. Part II: Implementation of a new snow parameterization. *Mon. Wea. Rev.*, **136**, 5095–5115, doi:10.1175/2008MWR2387.1.
- Varble, A., and Coauthors, 2011: Evaluation of cloud-resolving model intercomparison simulations using TWP-ICE observations: Precipitation and cloud structure. *J. Geophys. Res.*, **116**, D12206, doi:10.1029/2010JD015180.
- , and Coauthors, 2014: Evaluation of cloud-resolving and limited area model intercomparison simulations using TWP-ICE observations: 2. Precipitation microphysics. *J. Geophys. Res. Atmos.*, **119**, 13 919–13 945, doi:10.1002/2013JD021372.
- Willison, J., W. A. Robinson, and G. M. Lackmann, 2013: The importance of resolving mesoscale latent heating in the North Atlantic storm track. *J. Atmos. Sci.*, **70**, 2234–2250, doi:10.1175/JAS-D-12-0226.1.
- Xu, W., and S. A. Rutledge, 2015: Morphology, intensity, and rainfall production of MJO convection: Observations from DYNAMO shipborne radar and TRMM. *J. Atmos. Sci.*, **72**, 623–640, doi:10.1175/JAS-D-14-0130.1.
- Yanai, M., and R. H. Johnson, 1993: Impacts of cumulus convection on thermodynamic fields. *The Representation of Cumulus Convection in Numerical Models of the Atmosphere*, Meteor. Monogr., No. 46, Amer. Meteor. Soc., 39–62.
- , S. Esbensen, and J.-H. Chu, 1973: Determination of bulk properties of tropical cloud clusters from large-scale heat and moisture budgets. *J. Atmos. Sci.*, **30**, 611–627, doi:10.1175/1520-0469(1973)030<0611:DOBPOT>2.0.CO;2.
- Yang, S., and E. A. Smith, 1999: Four-dimensional structure of monthly latent heating derived from SSM/I satellite measurements. *J. Climate*, **12**, 1016–1037, doi:10.1175/1520-0442(1999)012<1016:FDSOML>2.0.CO;2.
- Yoneyama, K., C. Zhang, and C. N. Long, 2013: Tracking pulses of the Madden–Julian oscillation. *Bull. Amer. Meteor. Soc.*, **94**, 1871–1891, doi:10.1175/BAMS-D-12-00157.1.
- Zhang, C., and S. M. Hagos, 2009: Bi-modal structure and variability of large-scale diabatic heating in the tropics. *J. Atmos. Sci.*, **66**, 3621–3640, doi:10.1175/2009JAS3089.1.
- Zhang, M. H., and J. L. Lin, 1997: Constrained variational analysis of sounding data based on column-integrated budgets of mass, heat, moisture, and momentum: Approach and application to ARM measurements. *J. Atmos. Sci.*, **54**, 1503–1524, doi:10.1175/1520-0469(1997)054<1503:CVAOSD>2.0.CO;2.
- , —, R. T. Cederwall, and J. J. Yio, 2001: Objective analysis of ARM IOP data: Method and sensitivity. *Mon. Wea. Rev.*, **129**, 295–311, doi:10.1175/1520-0493(2001)129<0295:OAOAID>2.0.CO;2.
- Zipser, E. J., 1977: Mesoscale and convective-scale downdrafts as distinct components of squall-line structure. *Mon. Wea. Rev.*, **105**, 1568–1589, doi:10.1175/1520-0493(1977)105<1568:MACDAD>2.0.CO;2.